SAND2011-2740C

ILASS Americas, 23nd Annual Conference on Liquid Atomization and Spray Systems, Ventura, CA, May 2011

A Dense Fluid Approximation for the Simulation of Diesel Engine Fuel Injection Processes

Rainer N. Dahms[1], Joseph C. Oefelein and Lyle M. Pickett
Combustion Research Facility, Sandia National Laboratories, Livermore, CA 94551, USA

Abstract

A high-fidelity Large Eddy Simulation (LES) of the Sandia baseline non-reacting n-heptane experiment is performed (www.sandia.gov/ecn). The envelope of transient conditions in pressure, temperature, density, and mixture fraction space is studied using a real-gas model based on a 32-term BWR equation of state along with non-linear mixing rules to account for multi-component mixture states. These data reveal that many Diesel engine injection processes take place under transcritical thermodynamic conditions, where the fuel is supercritical with respect to pressure and subcritical with respect to temperature. Under such conditions, substantial thermodynamic non-idealities and transport anomalies exist. Mixture properties exhibit liquid-like densities, gas-like diffusivities, and pressure-dependent solubilities. The isothermal compressibility and constant pressure specific heat increase significantly. Heat of vaporization and surface tension diminish. Under these conditions the classical view of spray atomization and secondary breakup processes as an appropriate model comes into question. To account for these phenomena, we apply a dense fluid approximation using a multi-component formulation that applies to arbitrary hydrocarbon mixtures at near-critical and supercritical conditions. The model accounts for real fluid effects at low-temperature, high-pressure conditions typically observed in Diesel engine fuel mixing processes. Using this model, LES results are compared to the available experimental data of quantitative mixture fraction measurements by Rayleigh scattering. The simulations qualitatively reproduce key experimental features such as the flow structure and spatial evolution.

[1]Corresponding author

Introduction

Highly efficient ultra-low emission engines are in high demand due to rising petroleum-derived fuel prices and severe emission regulations. The Diesel engine offers a promising technological approach to meet these challenges. It achieves a superior thermal efficiency compared to gasoline engines due to higher applicable compression ratios. However, traditional Diesel engines are known to produce higher amounts of harmful emissions such as soot or nitric oxides than their gasoline counterparts. Substantial reductions of such emissions in Diesel engines require a comprehensive understanding of the complex interplay between fuel injection and turbulent combustion. Several experimental techniques such as Rayleigh-scattering, Mie-scattering, or Schlieren imaging have been developed to explore further details of the mixing process between the Diesel fuel and the ambient gas [1, 2, 3]. Additionally, substantial efforts have been made to develop fuel injection models that can be used in computational fluid dynamic (CFD) simulations. The classical view on these processes is that the liquid fuel undergoes primary breakup caused by unstable waves on the liquid surface. Due to the relative velocity between the gas and the liquid phase, the growth of the liquid wave instabilities lead to the formation of droplets, which eventually shear from the liquid surface. During the secondary breakup process, these droplets break down into even smaller ones and the main evaporation to fuel vapor takes place. This vapor then mixes up with the ambient hot gas to finally produce an ignitable mixture. Typically, these processes are modeled using a Kelvin/Helmholtz-Rayleigh/Taylor breakup model [4, 5, 6] and a multi-phase evaporation model such as in [7]. Such models are widely used in today's multi-dimensional simulation methods [8, 9, 10, 11, 12].

In this paper, a Large Eddy Simulation (LES) of the Sandia baseline non-reacting n-heptane experiment is performed. A rigorous thermodynamical analysis is presented using a real-gas model based on a 32-term BWR equation of state along with non-linear mixing rules to account for multi-component mixture states. Motivated by this analysis, a dense fluid approximation is proposed as a new model. The model equations are provided and simulation results are presented and compared to available experimental data.

Model Formulation

Results presented were obtained using the theoretical-numerical framework developed by Oefelein [13, 14]. The numerical framework solves the fully coupled conservation equations of mass, momentum, total-energy and species. For LES, the filtered version of the governing conservation equations are solved. These equations are given as:

$$\frac{\partial \overline{\rho}}{\partial t} + \nabla \cdot (\overline{\rho}\tilde{\mathbf{u}}) = 0, \tag{1}$$

$$\frac{\partial}{\partial t}(\overline{\rho}\tilde{\mathbf{u}}) + \nabla \cdot \left[\left(\overline{\rho}\tilde{\mathbf{u}} \otimes \tilde{\mathbf{u}} + \frac{\mathcal{P}}{M^2}\mathbf{I} \right) \right] = \nabla \cdot \vec{\vec{\mathcal{T}}}, \tag{2}$$

$$\begin{aligned} \frac{\partial}{\partial t}(\overline{\rho}\tilde{e}_t) \quad &+ \quad \nabla \cdot [(\overline{\rho}\tilde{e}_t + \mathcal{P})\tilde{\mathbf{u}}] \\ &= \quad \nabla \cdot \left[\left(\vec{\mathcal{Q}}_e + M^2(\vec{\vec{\mathcal{T}}} \cdot \tilde{\mathbf{u}}) \right) \right] + \overline{\dot{Q}}_e, \end{aligned} \tag{3}$$

$$\frac{\partial}{\partial t}(\overline{\rho}\tilde{Y}_i) + \nabla \cdot (\overline{\rho}\tilde{Y}_i\tilde{\mathbf{u}}) = \nabla \cdot \vec{\mathcal{S}}_i + \overline{\dot{\omega}}_i. \tag{4}$$

The terms $\mathcal{P}$, $\vec{\vec{\mathcal{T}}}$, $\vec{\mathcal{Q}}_e$ and $\vec{\mathcal{S}}_i$ represent respective composite (i.e., molecular plus *SGS*) stresses and fluxes. The terms $\overline{\dot{Q}}_e$ and $\overline{\dot{\omega}}_i$ represent the filtered energy and species source terms.

The subgrid-scale closure is obtained using the "mixed" dynamic Smagorinsky model by combining the models proposed by Erlebacher, Hussaini, Speziale and Zang [15] and Speziale [16] with the dynamic modeling procedure [17, 18, 19, 20, 21]. The composite stresses and fluxes in Eqs. (1)–(4) are given as

$$\begin{aligned} \vec{\vec{\mathcal{T}}} \quad &= \quad (\mu_t + \mu)\frac{1}{Re}\left[-\frac{2}{3}(\nabla \cdot \tilde{\mathbf{u}})\mathbf{I} + \left(\nabla\tilde{\mathbf{u}} + \nabla\tilde{\mathbf{u}}^T \right) \right] \\ &\quad -\overline{\rho}\left(\widetilde{\tilde{\mathbf{u}} \otimes \tilde{\mathbf{u}}} - \tilde{\mathbf{u}} \otimes \tilde{\mathbf{u}} \right), \end{aligned} \tag{5}$$

$$\begin{aligned} \vec{\mathcal{Q}}_e \quad &= \quad \left(\frac{\mu_t}{Pr_t} + \frac{\mu}{Pr} \right)\frac{1}{Re}\nabla\tilde{h} + \sum_{i=1}^{N} \tilde{h}_i\vec{\mathcal{S}}_i \\ &\quad -\overline{\rho}\left(\widetilde{\tilde{h}\tilde{\mathbf{u}}} - \tilde{\tilde{h}}\tilde{\mathbf{u}} \right), \text{ and} \end{aligned} \tag{6}$$

$$\vec{\mathcal{S}}_i \quad = \quad \left(\frac{\mu_t}{Sc_{t_i}} + \frac{\mu}{Sc_i} \right)\frac{1}{Re}\nabla\tilde{Y}_i - \overline{\rho}\left(\widetilde{\tilde{Y}_i\tilde{\mathbf{u}}} - \tilde{\tilde{Y}}_i\tilde{\mathbf{u}} \right). \tag{7}$$

The term μ_t represents the *SGS* eddy viscosity, given by

$$\mu_t = \overline{\rho}C_R\Delta^2\Pi_{\tilde{\mathbf{S}}}^{\frac{1}{2}}, \tag{8}$$

where

$$\Pi_{\tilde{\mathbf{S}}} = \tilde{\mathbf{S}} : \tilde{\mathbf{S}}, \text{ and } \tilde{\mathbf{S}} = \frac{1}{2}\left(\nabla\tilde{\mathbf{u}} + \nabla\tilde{\mathbf{u}}^T \right). \tag{9}$$

The terms C_R, Pr_t, and Sc_{t_i} represent the Smagorinsky, *SGS*-Prandtl and *SGS*-Schmidt numbers and are evaluated dynamically as functions of space and time. The overall model includes the Leonard and cross-term stresses and provides a Favre averaged generalization of the Smagorinsky eddy viscosity model [22] coupled with gradient diffusion models that simulate subgrid-scale mass and energy transport processes.

Thermodynamic and Transport Properties - The Dense Fluid Approximation

Our model provides a generalized treatment of the equation of state, thermodynamics, and transport processes for any arbitrary hydrocarbon mixture at near-critical and supercritical conditions. To account for thermodynamic non-idealities and transport anomalies over a wide range of pressures and temperatures, we apply an extended corresponding-states principle similar to that developed by Rowlinson and Watson [23] with two different equations of state. A 32-term Benedict-Webb-Rubin (*BWR*) equation of state is used to predict the pressure-volume-temperature (*PVT*) behavior of the liquid-phase, saturated vapor mixtures, and gas phase properties in the vicinity of the critical point. The Soave-Redlich-Kwong (*SRK*) equation of state [24, Chapter 3] is used elsewhere.

The law of corresponding-states expresses the generalization that equilibrium properties which depend on intermolecular forces are related to the critical properties in a universal way. In 1873, van der Waals showed that this law is theoretically valid for all pure substances whose *PVT* properties can be expressed in terms of a two-constant equation of state. In 1939, Pitzer showed that this law is similarly valid for substances which can be described by a two parameter intermolecular potential function. The corresponding-states principle holds well for fluids containing simple molecules and, upon semi-empirical extension, also holds for more complex mixtures.

The corresponding-states model used in this study is based on three assumptions: 1) the configurational properties of a single phase mixture η_m can be equated to those of a hypothetical pure fluid; i.e.,

$$\eta_m(\rho, T, X_1, \ldots, X_N) = \eta_x(\rho, T) \tag{10}$$

2) the properties of the hypothetical pure fluid obey classical two parameter corresponding-states formalism

$$\eta_x(\rho, T) = \eta_o F_\eta(W_o, W_x, \hbar_x, f_x) \tag{11}$$

where η_o corresponds to a reference fluid; and 3) the reference fluid density and temperature, ρ_o and T_o, obey an extended equilibrium corresponding-states principle given by

$$\rho_o = \rho \hbar_x \qquad T_o = T/f_x \tag{12}$$

The terms $\hbar_x$, f_x and W_x in Eqs. (10)–(12) are, respectively, the equivalent substance volume reducing ratio, the equivalent substance temperature reducing ratio, and molecular weight for the multi-component mixture. The equivalent substance volume reducing ratio accounts for the distribution of energy with respect to the reference fluid. The temperature reducing ratio accounts for molecular size differences. F_η in Eq. (11) is a dimensional scaling factor. The functional forms of these parameters are described below.

Implementation of the corresponding-states methodology requires the selection of a reference fluid. In this study methane is employed for two reasons. First, a reliable database exists with sufficient data correlated for the equation of state, relevant thermodynamic properties, and transport properties. Second, it is similar in structure to the chemical systems of interest.

To apply the model to mixtures, analytical expressions for F_η must be specified along with a set of mixing and combining rules for $\hbar_x$, f_x and W_x, a reference fluid equation of state, and relevant property data for the reference fluid. Following Leland and Chappelear [25], the mixing rules employed are as follows

$$\hbar_x = \sum_{i=1}^{N} \sum_{j=1}^{N} X_i X_j \hbar_{ij} \tag{13}$$

$$f_x = \hbar_x^{-1} \sum_{i=1}^{N} \sum_{j=1}^{N} X_i X_j f_{ij} \hbar_{ij} \tag{14}$$

$$W_x^{n/2} f_x^{1/2} \hbar_x^{-4/3} = \sum_{i=1}^{N} \sum_{j=1}^{N} X_i X_j W_{ij}^{n/2} f_{ij}^{1/2} \hbar_{ij}^{-4/3} \tag{15}$$

where subscript ij corresponds to binary pair parameters. Combining rules for these terms are given by

$$\hbar_{ij} = \frac{1}{8} \left(\hbar_i^{1/3} + \hbar_j^{1/3} \right)^3 (1 - \ell_{ij}) \tag{16}$$

$$f_{ij} = (f_i f_j)^{\frac{1}{2}} (1 - k_{ij}) \tag{17}$$

$$W_{ij} = \frac{2 W_i W_j}{W_i + W_j} \tag{18}$$

In Eqs. (16) and (17), the quantities l_{ij} and k_{ij} represent binary interaction parameters which account for molecular energy and volumetric effects in the binary system. The quantities $\hbar_i$ and f_i are the equivalent substance reducing ratios for compound i in the mixture. These quantities are obtained by a two-parameter methodology as follows

$$\hbar_i = \left(\frac{V_{c,i}}{V_{c,o}} \right) \phi_i(V_{r,i}, T_{r,i}, \omega_i) \tag{19}$$

$$f_i = \left(\frac{T_{c,i}}{T_{c,o}}\right)\theta_i(V_{r,i}, T_{r,i}, \omega_i) \tag{20}$$

Functions ϕ_i and θ_i are shape factors [26, 27] which account for non-sphericity with respect to molecular structure. Subscript c denotes a critical value, r a reduced value.

The functional form of the *BWR* equation of state is

$$p(\rho,T) = \sum_{n=1}^{9} a_n(T)\rho^n + \sum_{n=10}^{15} a_n(T)\rho^{2n-17}\exp -\gamma\rho^2 \tag{21}$$

where γ is an empirically fitted parameter termed the strain rate. Coefficients a_n are functions of temperature and the universal gas constant R_u. These quantities are given as

$$\begin{aligned}
a_1(T) &= R_u T \\
a_2(T) &= N_1 T + N_2 T^{1/2} + N_3 + N_4/T + N_5/T^2 \\
a_3(T) &= N_6 T + N_7 + N_8/T + N_9/T^2 \\
a_4(T) &= N_{10} T + N_{11} + N_{12}/T \\
a_5(T) &= N_{13} \\
a_6(T) &= N_{14}/T + N_{15}/T^2 \\
a_7(T) &= N_{16}/T \\
a_8(T) &= N_{17}/T + N_{18}/T^2 \\
a_9(T) &= N_{19}/T^2 \\
a_{10}(T) &= N_{20}/T^2 + N_{21}/T^3 \\
a_{11}(T) &= N_{22}/T^2 + N_{23}/T^4 \\
a_{12}(T) &= N_{24}/T^2 + N_{25}/T^3 \\
a_{13}(T) &= N_{26}/T^2 + N_{27}/T^4 \\
a_{14}(T) &= N_{28}/T^2 + N_{29}/T^3 \\
a_{15}(T) &= N_{30}/T^2 + N_{31}/T^3 + N_{32}/T^4
\end{aligned}$$

The *SRK* equation is of the form

$$p(\rho,T) = \frac{\rho R_u T}{1-\rho b} - \frac{\rho^2 a}{1+\rho b} \tag{22}$$

where

$$a = \frac{\Omega_a R_u^2 T_c^2}{p_c}\left[1 + f\omega(1 - T_r^{1/2})\right]^2 \qquad b = \frac{\Omega_b R_u T_c}{p_c}$$

and

$$f\omega = 0.48 + 1.57\omega - 0.176\omega^2$$

Here, ω represents the acentric factor and Ω_a and Ω_b are empirically derived constants. When evaluated with respect to *bar*, $mol/liter$, and K, these constants take on the values of 0.42748 and 0.086640, respectively. Equation (12) coupled with Eq. (21) in the vicinity of the critical point, Eq. (22) elsewhere, and the mixing rules given by Eqs. (13)–(15) are used to obtain the *PVT* behavior for the multi-component system considered in this study.

Explicit expressions for the enthalpy, Gibbs energy, and constant pressure specific heat are required as a function of temperature and pressure. Having established an analytical representation for real mixture *PVT* behavior, these properties are obtained using a two step process. First, respective reference properties are transformed to those for the mixture at a given pressure using the corresponding-states methodology outlined above. The equation of state is then employed to obtain a pressure correction using departure functions of the form given by Eqs. (24)–(25) [24]. These functions describe the deviation of known reference values with respect to pressure at a given temperature and composition. They are derived by means of the Maxwell relations [28, Chapter 10].

The viscosity μ and thermal conductivity λ are obtained using the methodologies developed by Ely and Hanley [29, 30]. Equations (10)–(18) are employed with scaling factors of the form

$$F_\mu = \left(\frac{W_x}{W_o}\right)^{\frac{1}{2}} f_x^{\frac{1}{2}} \hbar_x^{-\frac{2}{3}} \tag{26}$$

$$F_\lambda = \left(\frac{W_o}{W_x}\right)^{\frac{1}{2}} f_x^{\frac{1}{2}} \hbar_x^{-\frac{2}{3}} \tag{27}$$

using values of $n = 1$ and $n = -1$, respectively, in Eq. (15).

For mixtures of molecules of substantially different size; i.e., when the difference between two binary species approaches volumetric ratios on the order $V_{c,1}/V_{c,2} \sim 6$, the mean density approximation given by Eq. (10) fails. Since most thermo-physical properties are determined from relatively short range forces, the properties of the larger component dominate. To correct for this effect in the prediction of mixture viscosity, Eq. (26) is used together with an Enskog correction of the form given by Ely and Hanley [29]

$$\mu = \mu_o(\rho_o, T_o)F_\mu + \Delta\mu^{ENSKOG} \tag{28}$$

This correction has been shown to improve predictions for mixtures which exhibit large size and mass differences for both dense and dilute gas states.

In a similar manner, Ely and Hanley [30] propose an expression of the form

$$\lambda = \lambda_o(\rho_o, T_o)F_\lambda + \lambda''(T) + \Delta\lambda_{crit}(\rho,T) \tag{29}$$

for thermal conductivity. The first term on the right-hand side accounts for purely collisional and transitional effects. The second term accounts for transfer of energy due to internal degrees of freedom. This term is modeled by means of a modified Eucken correlation with an empirical mixing rule for polyatomic gases [24]. The last term in Eq. (29) accounts for near critical effects.

The effective diffusion coefficient $\mathcal{D}_{im}$ for each species i is related to the binary diffusion coefficients $\mathcal{D}_{ij}$ of the

$$\Delta H = -\int_{\infty}^{V}\left(p-\frac{RT}{V}\right)dV + T\int_{\infty}^{V}\left[\left(\frac{\partial p}{\partial V}\right)_V - \frac{R}{V}\right]dV + RT(Z-1) \quad (23)$$

$$\Delta G = -\int_{\infty}^{V}\left(p-\frac{RT}{V}\right)dV - RT\ln\left(\frac{V}{V_o}\right) + RT(Z-1) \quad (24)$$

$$\Delta C_p = T\int_{\infty}^{V}\left(\frac{\partial^2 p}{\partial T^2}\right)dV - \frac{T(\partial p/\partial V)_V^2}{(\partial p/\partial V)_T} - R \quad (25)$$

mixture using the formula given by Bird [31, Chapter 16]

$$\mathcal{D}_{im,g} = \frac{(1-X_i)}{\sum_{\substack{j=1\\ j\neq i}}^{N}\left(\frac{X_j}{\mathcal{D}_{ij}}\right)} \quad (30)$$

Theory describing diffusion in binary gas mixtures at low to moderate pressures has been well developed [24]. At low pressures, these coefficients vary inversely with pressure or density and are essentially independent of composition. At high pressure, however, the product $\mathcal{D}_{ij}p$ (or $\mathcal{D}_{ij}\rho$) is no longer constant. For this situation, these products decrease with increasing pressure (or density) and are dependent on composition. Thus, binary mass diffusivities are obtained by means of a two step approach. First, low-pressure theory is employed using Chapman-Enskog theory coupled with the Lennard-Jones intermolecular potential functions. A high pressure correction is then applied using the corresponding-states methodology proposed by Takahashi [32].

Numerical Method

Calculations were performed using the massively parallel RAPTOR code framework developed by Oefelein [13]. Unlike conventional LES solvers, RAPTOR is essentially a DNS solver that has been optimized to meet the strict algorithmic requirements imposed by the LES formalism. The theoretical framework solves the fully coupled conservation equations of mass, momentum, total-energy and species for a chemically reacting flow system for both multi-component and mixture-averaged systems. It is designed to handle high-Reynolds-number, high-pressure, real-gas and liquid conditions over a wide Mach operating range (from incompressible to supersonic conditions). It also accounts for detailed chemistry, thermodynamics and transport processes at the molecular level and is sophisticated in its ability to handle a generalized subgrid-scale model framework. The model framework is capable of treating multi-phase flows, spray combustion processes and/or particulates such as soot using a Lagrangian-Eulerian formulation. The numerical formulation treats the compressible form of the conservation equations but can be evaluated efficiently in the incompressible limit. It handles complex geometries and time-varying grids in generalized coordinates using the Arbitrary Lagrangian Eulerian (ALE) formulation. Representative case studies are given by Oefelein *et al.* [33, 34, 35, 36, 37, 38, 39].

The temporal integration scheme employs an all Mach number formulation using the dual-time stepping technique with generalized preconditioning. The approach is 4th order accurate in time and provides a fully-implicit solution using a fully explicit and highly-scalable multi-stage scheme in pseudo-time. Preconditioning is applied in the inner "pseudo-time" loop and coupled to local time-stepping techniques to minimize convective, diffusive, geometric, and source term anomalies (i.e., stiffness) in an optimal manner. This, in turn, maximizes convergence rates as the system is advanced forward in time. The formulation is A-stable, which allows one to set the physical-time step based solely on accuracy considerations. This attribute alone typically provides a 2 to 3 order of magnitude increase in the allowable integration time-step compared to other methods, especially in the incompressible, low Mach number limit.

The spatial scheme is designed using non-dissipative, discretely-conservative, staggered, finite-volume differencing stencils. The discretization is formulated in generalized curvilinear coordinates and employs a general R-refinement adaptive mesh (AMR) capability. This allows us to account for the inherent effects of geometry on turbulence over the full range of relevant scales while significantly reducing the total number of grid cells required in the computational domain. Treating the full range of scales is a critical requirement since turbulence-chemistry interactions are inherently coupled through a cascade of nonlinear interactions between the largest and smallest scales of the flow.

The differencing methodology has been specifically designed for LES. In particular, the 2nd order accurate staggered grid formulation, where we store scalar values at cell centers and velocity components at respective cell faces, fulfills two key accuracy requirements. First, the staggered formulation is spatially non-dissipative (i.e., possess purely imaginary Fourier characteristics), which eliminates numerical contamination of the subgrid-scale models due to artificial dissipation. Second, the stencils provide discrete conservation of mass, momentum, total

energy and species, which is an imperative requirement for LES. This eliminates the artificial build up of velocity and scalar energy at the high wave-numbers, which causes both accuracy problems and numerical instabilities in turbulent flow calculations.

The numerical algorithm has been designed using a fully consistent and generalized treatment for boundary conditions based on the method of characteristics. The combined formulation allows us to treat complex time-varying IC-engine geometries in a routine manner. The code has been simultaneously optimized to provide excellent parallel scalability attributes using a distributed multi-block domain decomposition with completely general connectivity. The superior scalability attributes demonstrated (both strong and weak) are a direct result of the explicit nature of the code. The algorithm is also fully vectorized and has been optimized for commodity architectures.

Computational Setup

To establish an initial baseline for comparisons, calculations were performed using a simple computational domain that is of the same size as the experimental combustion vessel. The domain consists of a $d = 0.1$ *mm* injector nozzle placed at the head end of a square chamber that is 1000 nozzle diameters cubed. The initial conditions of the combustion vessel are given in Table 1. The current calculations were performed using a grid that contained $576 \times 144 \times 144$ cells in the x, y and z directions, respectively. The grid is stretched to provide appropriate resolution in the near-jet region where steep gradients appear. The n-heptane jet is injected in the axial direction, parallel to the x axis. No-slip wall conditions were imposed everywhere in the chamber. Correlated fluctuations were imposed at the inflow boundary (as explained in Ref. [40]) based on the assumption that the turbulent boundary layer followed a 1/7th power law profile in the mean as it developed. The transient jet pulse was simulated to closely approximate the actual experimental conditions. Start of injection began at $t = 0$ *ms*, and ramped up to a mass flow of 2.7 mg/ms in 0.03 *ms* as shown in Fig. 1. At the current injection conditions, this produces a bulk velocity of 554 m/s and a corresponding jet Reynolds number of $150,000$. The quasi-steady portion of the pulse lasted for 6.66 *ms*. At $t = 6.69$ *ms*, the jet was ramped down to zero velocity, with the end of injection occurring at $t = 6.93$ *ms*. The calculations were parallelized by decomposing the computational domain into 864 blocks and run on a local cluster. Total integration time was 8 *ms* using a time-step of 2 *ns*.

Chamber pressure	43.3 bar
Fuel (C_7H_{16}) injection temperature	373 K
Chamber gas temperature	1000 K
X_{N_2}	0.8971
X_{CO_2}	0.0652
X_{H_2O}	0.0377
X_{O_2}	0.0
$\|\|\vec{u}\|\|$	≈ 0 m/s
Injected fuel mass	18.3 mg
Ambient gas density	14.57 kg/m^3

Table 1: Initial conditions of the Sandia non-reacting n-heptane experiment. Mole fractions of the ambient gas components are given. The bulk flow velocity magnitude $||\vec{u}||$ and its turbulent kinetic energy are negligibly small before the start of injection.

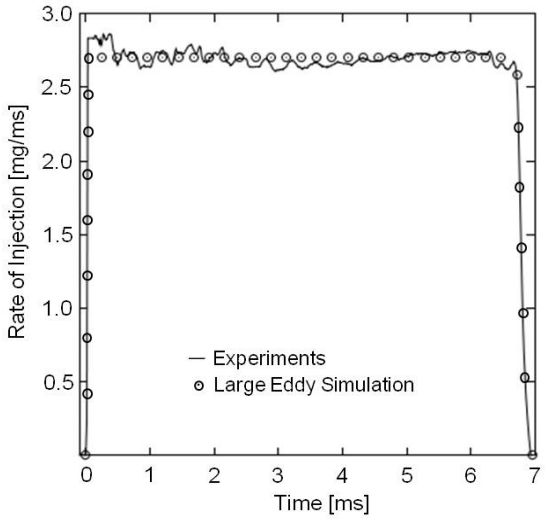

Figure 1: Comparisons of the rate of fuel injection obtained from experiments and simulation.

Experimental Setup

The Sandia baseline n-heptane experiment is performed in the optically accessible, constant-volume combustion vessel designed for Diesel combustion experiments. Here we focus on the non-reacting conditions cited by Pickett *et al.* [41], where various schematics and photographs of the setup can also be found. Fuel is injected with an electronically controlled common rail injector at a pressure of 154.33 *MPa* and 373 *K*. The ambient gas composition in the vessel was conditioned to provide an inert composition of N_2, CO_2, and H_2O. The

actual mole fractions of these components are summarized in Table 1. The corresponding molecular weight is $M = 28.68\ g/mol$. Inert conditions were used to focus on primary issues related to thermodynamics and transport.

Results and Discussion

To obtain a concise and comprehensive analysis of the fuel mixing process, the mixture fraction variable is introduced as

$$Z = \frac{m_1}{m_1 + m_2} \quad , \tag{31}$$

with m_1 as the fuel stream mass and m_2 as the oxidizer stream mass, respectively. Using this definition, $Z = 0$ refers to the composition of the oxidizer stream (N_2-CO_2-H_2O) and $Z = 1$ refers to the composition of the corresponding fuel stream (C_7H_{16}). This is exemplified in Fig. 2(top), which shows a Rayleigh-scattering image of the investigated Sandia n-heptane case. A scatter plot of mixture temperatures, conditioned on the mixture fraction variable, is shown in Fig. 2(bottom). This data has been processed from a companion LES using the dense fluid approximation described above. The scatter plot reveals only slight mean distributions of the mixture temperature. This allows one to associate this temperature to the mixture fraction variable as expressed by the best fit mixture temperature line also shown in Fig. 2(bottom).

To investigate the envelope of thermodynamic mixture conditions during the Sandia n-heptane fuel injection mixing process, the N_2-H_2O-CO_2/C_7H_{16} multi-component mixture space is considered by extending the classical P-V-T phase diagram of pure components to a 4D pressure-temperature-density-mixture fraction (P-T-ρ-Z) phase diagram of oxidizer and fuel streams. The corresponding P-T-Z mixture space is presented in Fig. 3. Corresponding density values, computed by the 32-term BWR mixture state equation, are exemplarily provided for the two cut planes at $Z = 0$ and $Z = 1$, respectively.

The BWR mixture state equation computes pseudo-pure vapor/liquid phase transitions, assuming that the composition of the mixture does not change during a phase transition ($x' = x''$; x': Liquid mole fraction; x'': Vapor mole fraction). Therefore, the bubble point and dew point curves of the multi-component N_2-H_2O-CO_2 oxidizer stream collapse into a single curve (pseudo-pure fluid bubble/dew point curve in Fig. 3). Such pseudo-pure fluid bubble/dew points are processed for each mixture fraction state and the envelope of these points is shown in Fig. 4. Corresponding multi-component bubble and dew point curves can be calculated with this method from vapor-liquid-equilibrium calculations. However,

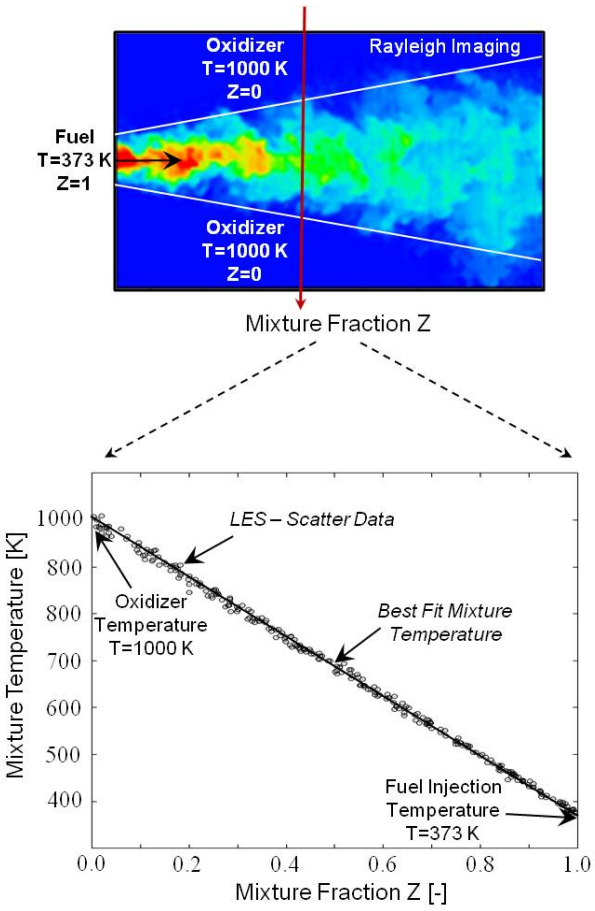

Figure 2: Rayleigh-scattering image of the Sandia n-heptane case (top) and a scatter plot/line of best fit of temperature-mixture fraction variables (bottom) processed from a LES using the dense fluid approximation for Diesel fuel injection mixing processes presented in this paper.

for the sake of clarity, only the pseudo-pure fluid bubble/dew point curves are shown in Fig. 4. It is important to realize that the critical mixing line, defined as the envelope of critical temperatures $T = T_{Crit}(Z)$ and pressures $p = p_{Crit}(Z)$ for each mixture state Z, can be accurately computed from the pseudo-pure fluid model. Since bubble and dew points merge at the critical point, the implicitly applied pseudo-pure fluid model assumption $x' = x''$ is fulfilled for a multi-component mixture at its critical point. With such a defined critical mixing line, the thermodynamic regimes of liquid, compressed liquid, vapor, ideal gas, and the supercritical state can be defined as shown in Fig. 4.

In the following, the mixture critical pressures and mixture critical temperatures are processed from the critical mixing line defined in Fig. 4 as a function of the mixture fraction variable. Results are presented in Figs. 5

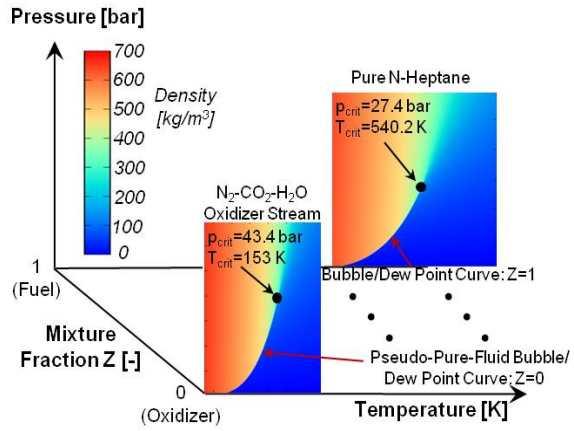

Figure 3: Pressure-temperature-density-mixture fraction (P-T-ρ-Z) space defined by mixtures of the N_2-H_2O-CO_2 oxidizer stream (Z=0) and the C_7H_{16} fuel stream (Z=1). Density values have been obtained by the 32-term BWR mixture state equation. This equation of state computes pseudo-pure vapor/liquid phase transitions ($x' = x''$). Multi-component bubble and dew point curves can be obtained from Vapor-Liquid-Equilibrium (VLE) calculations. Critical points are shown for $Z = 0$ and $Z = 1$, respectively.

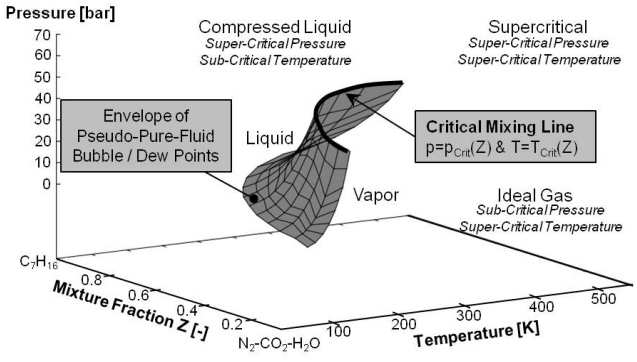

Figure 4: Visualization of the multi-component P-T-Z mixture space and the corresponding thermodynamic regimes. Multi-component bubble and dew point curves can be calculated from VLE calculations. For the sake of clarity, however, only the pseudo-pure fluid bubble/dew point curve envelope is shown here. The critical mixing line, defined as the envelope of critical temperatures $T = T_{Crit}(Z)$ and pressures $p = p_{Crit}(Z)$ for each mixture state, is appropriately captured by the pseudo-pure fluid mixture model.

and 6, respectively. For comparison, the critical pressures and temperatures of the pure components are summarized in Table 2. Both mixture critical properties are shown to be non-linear functions of the mixture fraction.

Component	Critical Temperature	Critical Pressure
C_7H_{16}	540 K	27.4 bar
N_2	126 K	33.9 bar
CO_2	304.2 K	73.8 bar
H_2O	647.1 K	220.6 bar

Table 2: Critical temperatures and pressures of the pure components involved in this study.

Since the mixture temperature can be assigned to the mixture fraction variable, compare Fig. 2, this mixture temperature is laid on top of the mixture critical temperature, as shown in Fig. 6. At a mixture fraction below $Z = Z^\star \approx 0.88$, this mixture temperature exceeds the mixture critical temperature of the corresponding mixture state.

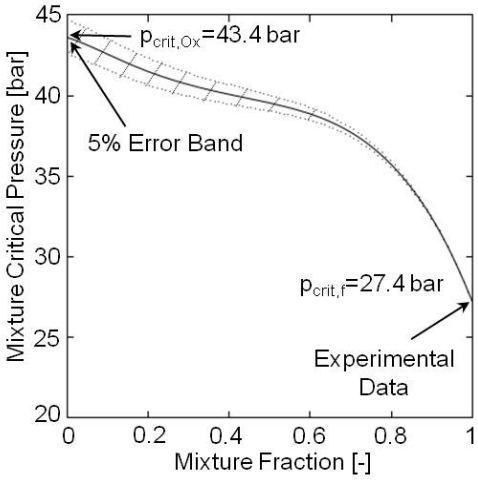

Figure 5: Mixture critical pressure $p_{Crit}(Z)$ as a function of the mixture fraction.

These results emphasize that the location of the mixture critical point is determined by non-linear mixing rules of the pure component critical properties. In turn, this analysis reveals that the concept of partial pressures p_i is only defined for ideal thermodynamic systems and their relation to the pure component critical pressures ($p_i \geq p_{i,crit}$) fails to qualitatively predict supercritical mixture states. The same conclusion can be obtained from the mathematical definition of the critical point. The critical point defines the limit of diffusion stability of the mixture, expressed for a binary mixture by

$$\left(\frac{\partial^2 g}{\partial X^2}\right)_{p,T} = \left(\frac{\partial^3 g}{\partial X^3}\right)_{p,T} = 0 \quad , \tag{32}$$

where g is the Gibbs molar energy of the mixture. In

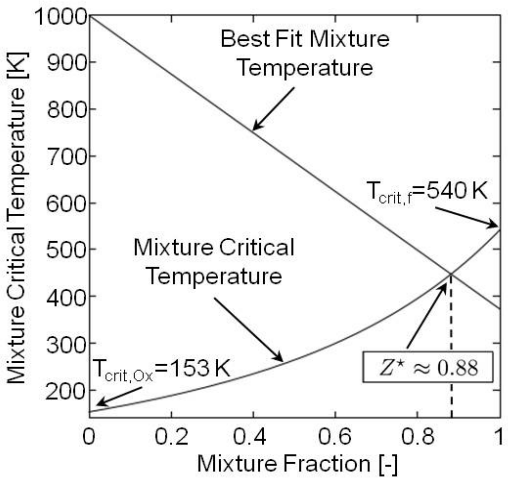

Figure 6: Mixture critical temperature $T_{Crit}(Z)$ as a function of the mixture fraction. For a mixture fraction below $Z = Z^\star \approx 0.88$, the best fit mixture temperature, taken from Fig. 2, exceeds the mixture critical temperature of that mixture state.

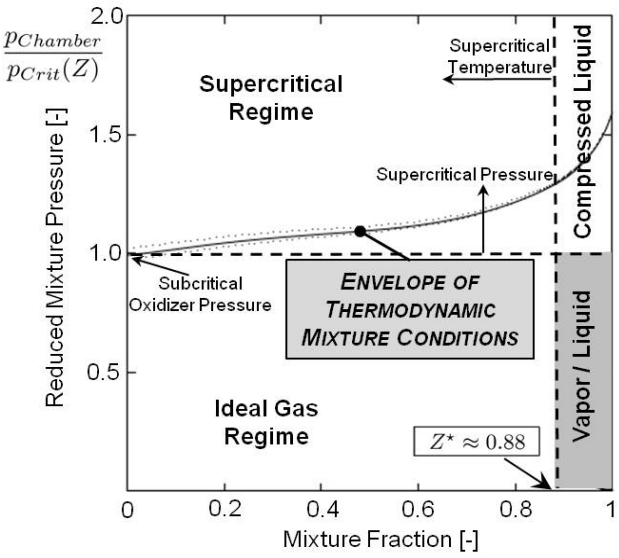

Figure 7: Envelope of the Sandia n-heptane fuel injection mixing process in a thermodynamic regime diagram. The constant chamber pressure ($p_{Chamber} = 43.3$ bar) exceeds the mixture critical pressure for all mixtures except of states close to $Z = 0$. However, at mixtures below $Z = Z^\star \approx 0.88$, the local mixture temperature exceeds the mixture critical temperature, compare Fig. 6. Therefore, the highlighted regime of first order phase transitions (liquid/vapor) has no meaning for the investigated Sandia n-heptane fuel injection mixing process.

the vicinity of the critical point, these equations can be derived in a Taylor series as follows

$$\Delta\left(\frac{\partial^2 g}{\partial X^2}\right)_{p,T} \approx \frac{\partial}{\partial T}\left(\frac{\partial^2 g}{\partial X^2}\right)_{p,T}\Delta T + \frac{\partial}{\partial p}\left(\frac{\partial^2 g}{\partial X^2}\right)_{p,T}\Delta p \qquad (33)$$

and

$$\Delta\left(\frac{\partial^3 g}{\partial X^3}\right)_{p,T} \approx \frac{\partial}{\partial T}\left(\frac{\partial^3 g}{\partial X^3}\right)_{p,T}\Delta T + \frac{\partial}{\partial p}\left(\frac{\partial^3 g}{\partial X^3}\right)_{p,T}\Delta p \qquad (34)$$

These two conditions can be used to compute the mixture critical temperatures and pressures of various binary mixtures such as in [42].

In Fig. 7, the envelope of the Sandia n-heptane fuel injection mixing process is investigated in a thermodynamic regime diagram. The reduced mixture critical pressure $p_{Chamber}/p_{Crit}(Z)$ as a function of the mixture fraction variable is shown. The constant chamber pressure is denoted by $p_{Chamber} = \text{const} = 43.3$ bar and the mixture critical pressure, taken from Fig. 5, is denoted by $p_{Crit}(Z)$, respectively. Supercritical mixture pressures are then defined as $p_{Chamber}/p_{Crit}(Z) > 1.0$. Supercritical mixture temperatures are found for mixture fractions below $Z = Z^\star \approx 0.88$. The available envelope of thermodynamic mixture conditions comprises the compressed liquid, supercritical, and ideal gas regimes. This analysis reveals that the fuel/oxidizer mixture only undergoes second order phase transitions. The mixing pathway does not cross the highlighted regime of first order phase transitions between liquid and vapor, however, for the conditions of interest. This thermodynamic analysis motivated the development of the dense fluid approximation as a new model for Diesel engine fuel injection mixing processes.

The thermodynamic analysis and model development has been performed using the 32-term BWR equation of state. For the sake of computational efficiency, the more efficient Soave-Redlich-Kwong (SRK) cubic equation of state along with appropriate mixing rules to consider multi-component mixture states has been applied for the LES of the Sandia n-heptane fuel injection mixing process. Figure 8 presents a comparison of predicted compressibility factors using the 32-term BWR and the SRK cubic equation of state for the envelope of thermodynamic mixture conditions, highlighted in Fig. 7. Except for the dense core region ($Z > 0.8$), the cubic equation of state is in good agreement with the more precise 32-term BWR state equation. For mixture fractions below $Z = Z' \approx 0.6$, the P-V-T behavior of the mixture ap-

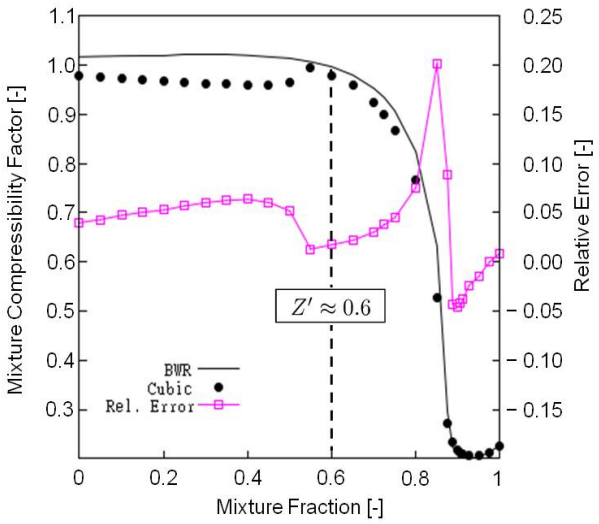

Figure 8: Comparison of predicted compressibility factors using the BWR and the SRK cubic equation of state for the envelope of thermodynamic mixture conditions, highlighted in Fig. 7. For mixture fractions below $Z = Z' \approx 0.6$, the P-V-T fluid behavior approaches the ideal gas limit.

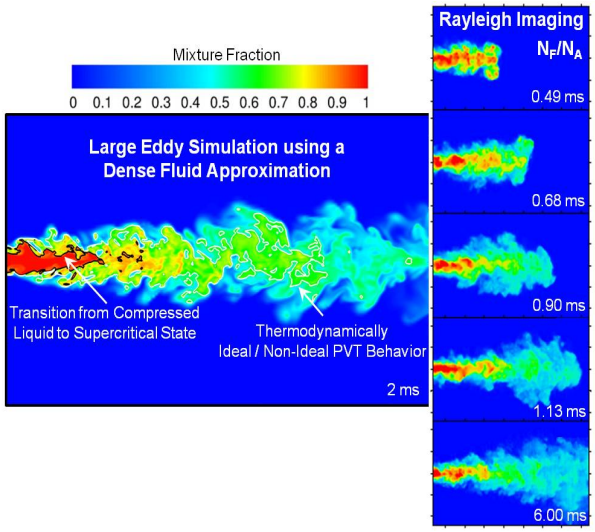

Figure 9: Qualitative comparison of predicted mixture fraction distributions, processed from a LES using the new dense fluid approximation model for Diesel engine fuel injection mixing processes (left) and experimental Rayleigh images (right) showing N_F/N_A. The two iso-lines in the simulation image mark the separation between regions of non-ideal/ideal fluid P-V-T behavior (white) as well as the transition from compressed liquid to supercritical mixture states (black) as analyzed in Figs. 7 and 8, respectively.

proaches the ideal gas limit. Figure 9 shows a qualitative comparison of predicted mixture fraction distributions, processed from a LES using the new model (left) and experimentally obtained ratios of N_F/N_A from Rayleigh-scattering images (right). The simulation qualitatively reproduces key characteristic features as the flow structure and spatial evolution. Two iso-lines are shown in Fig. 9(left). The white iso-line ($Z = Z' \approx 0.6$) highlights the separation between regions of thermodynamically ideal and non-ideal P-V-T fluid behavior. The black iso-line ($Z = Z^\star \approx 0.88$) represents the transition region from compressed liquid to supercritical mixture states, based on the analysis presented in Fig. 7. According to this analysis, substantial regions of the n-heptane jet are dictated by distinctive thermodynamic non-idealities and transport anomalies. In turn, this demands an enhanced treatment of Diesel engine fuel injection mixing processes by a real-gas dense fluid approximation, as presented in this paper.

Conclusions

A rigorous thermodynamic analysis has shown that the location of the critical mixing line in the introduced P-T-ρ-Z space is determined by non-linear mixing rules of the pure component critical properties. Its prediction requires a complex equation of state along with appropriate mixing rules. The classical approach of a partial pressure concept, as only applicable in the ideal gas limit, and its relation to pure component critical pressures ($p_i \geq p_{i,crit}$) fails to qualitatively predict such critical mixture states. Informed by this analysis, the envelope of thermodynamic mixture conditions of the Sandia baseline non-reacting n-heptane experiment is studied, using a Large Eddy Simulation along with the presented 32-term BWR real-gas mixture model. This model fully captures the P-T-ρ-Z behavior of arbitrary multi-component hydrocarbon mixtures at near critical and super-critical conditions when no first order phase transitions between liquid and vapor occur.

The generated data reveals that, under the conditions here, the envelope of thermodynamic mixture conditions ranges from a compressed liquid state of the fuel as it enters the combustion chamber to supercritical mixture conditions as the fuel mixes up with the oxidizer. First order phase transitions between liquid and vapor, however, do not occur and a vapor-liquid-equilibrium does not exist. Therefore, phenomena related to surface tension effects like primary and secondary breakup processes or fuel evaporation, and corresponding latent heats, have no meaning on the fuel injection process. Under these conditions, the classical view of spray atomization as an appropriate conception for Diesel engine

fuel mixing phenomena comes into question. A similar set of thermodynamic conditions is also anticipated for more realistic and complex Diesel fuels, since their critical properties are comparable to those of n-heptane.

Motivated by this analysis, a dense fluid approximation, accounting for the substantial thermodynamic non-idealities and transport anomalies of high-pressure and low-temperature fuel injection processes, is proposed as a new model for the simulation of Diesel engine fuel injection mixing processes. It does not include a particle model since the formation of fuel droplets is completely suppressed under the conditions investigated. This new model qualitatively reproduces key experimental features such as the flow structure and spatial evolution shown in Rayleigh-scattering images.

Acknowledgements

Support provided by the U.S. Department of Energy, Office of Energy Efficiency and Renewable Energy, Vehicle Technologies Program, is gratefully acknowledged. This research was performed at the Combustion Research Facility, Sandia National Laboratories, Livermore, California. Sandia is a multiprogramming laboratory operated by the Sandia Corporation, a Lockheed Martin Company, for the United States Department of Energy's National Nuclear Security Administration under contract DE-AC-94AL85000.

References

[1] Dennis L. Siebers. Liquid-Phase-Fuel Penetration in Diesel Sprays. *SAE Paper 980809*, 1998.

[2] J.D. Naber and D.L. Siebers. Effects of gas density and vaporization on penetration and dispersion of diesel sprays. *SAE Paper 960034*, 1996.

[3] John Abraham and Lyle Pickett. Computed and Measured Fuel Vapor Distribution in a Diesel Spray. *Atomization and Sprays*, 20:241–250, 2010.

[4] R.D. Reitz. Modeling atomization processes in high pressure vaporizing sprays. *Atomization and Sprays*, 3:309–337, 1987.

[5] S.C. Kong, P.K. Senecal, and R.D. Reitz. Development in Spray Modeling in Diesel and Direct-Injection Gasoline Engines. *Oil & Gas Sci. Techn.*, 54:197–204, 1999.

[6] S.C. Kong and R.D. Reitz. Use of Detailed Chemical Kinetics to Study HCCI Engine Combustion with Consideration of Turbulence Mixing Effects. *ASME Journal of Gas Turbines and Power*, 124:702–707, 2002.

[7] C. Crowe, M. Sommerfield, and Y. Tsuji. Multiphase Flows with Droplets and Particles. *CRC Press LLC*, 1998.

[8] Gokul Vishwanathan and R.D. Reitz. Numerical Predictions of Diesel Flame Lift-Off Length and Soot Distributions under Low Temperature Combustion Conditions. *SAE Paper 2008-01-1331*, 2008.

[9] S. Som and S.K. Aggarwal. Effects of Primary Breakup Modeling on Spray and Combustion Characteristics of Compression Ignition Engines. *Combust. Flame*, 157:1179–1193, 2010.

[10] T. Lucchini, G. D'Errico, D. Ettorre, and G. Ferrari. Numerical Investigation of Non-Reacting and Reacting Diesel Sprays in Constant-Volume Vessels. *SAE Paper 2009-01-1971*, 2009.

[11] T. Lucchini, G. D'Errico, and D. Ettorre. Numerical Investigation of the Spray-Mesh-Turbulence Interactions for High-Pressure, Evaporating Sprays at Engine Conditions. *Intl. J. Heat and Fluid Flow*, 32:285–297, 2011.

[12] F.P. Kärrholm and F. Tao. Three-Dimensional Simulation of Diesel Spray Ignition and Flame Lift-Off using OpenFOAM and KIVA-3V CFD Codes. *SAE Paper 2008-01-0961*, 2008.

[13] J. C. Oefelein. Large eddy simulation of turbulent combustion processes in propulsion and power systems. *Progress in Aerospace Sciences*, 42(1):2–37, 2006.

[14] J. C. Oefelein. *Simulation and Analysis of Turbulent Multiphase Combustion Processes at High Pressures*. PhD thesis, The Pennsylvania State University, University Park, Pennsylvania, May 1997.

[15] G. Erlebacher, M. Y. Hussaini, C. G. Speziale, and T. A. Zang. Toward the large eddy simulation of compressible turbulent flows. *J. Fluid Mech.*, 238:155–185, 1992.

[16] C. G. Speziale. Galilean invariance of subgrid-scale stress models in the large eddy simulation of turbulence. *J. Fluid Mech.*, 156:55–62, 1985.

[17] M. Germano, U. Piomelli, P. Moin, and W. H. Cabot. A dynamic subgrid-scale eddy viscosity model. *Phys. Fluids*, 3(7):1760–1765, 1991.

[18] P. Moin, K. Squires, W. Cabot, and S. Lee. A dynamic subgrid-scale model for compressible turbulence and scalar transport. *Phys. Fluids*, 3(11):2746–2757, 1991.

[19] D. K. Lilly. A proposed modification of the germano subgrid-scale closure method. *Phys. Fluids*, 3(11):633–635, 1992.

[20] Y. Zang, R. L. Street, and J. R. Koseff. A dynamic mixed subgrid-scale model and its application to turbulent recirculating flows. *Phys. Fluids*, 5(12):3186–3195, 1993.

[21] B. Vreman, B. Geurts, and H. Kuerten. On the formulation of the dynamic mixed subgrid-scale model. *Phys. Fluids*, 6(12):4057–4059, 1994.

[22] J. Smagorinsky. General circulation experiments with the primitive equations. I. The basic experiment. *Monthly Weather Review*, 91:99–164, 1963.

[23] J. S. Rowlinson and I. D. Watson. The prediction of the thermodynamic properties of fluids and fluid mixtures–I. The principle of corresponding states and its extensions. *Chem. Eng. Sci.*, 24(8):1565–1574, 1969.

[24] R. C. Reid, J. M. Prausnitz, and B. E. Polling. *The Properties of Liquids and Gases*. McGraw-Hill, New York, New York, 4th edition, 1987.

[25] T. W. Leland and P. S. Chappelear. The corresponding states principle. A review of current theory and practice. *Industrial and Engineering Chemistry Fundamentals*, 60(7):15–43, 1968.

[26] G. D. Fisher and T. W. Leland. Corresponding states principle using shape factors. *Industrial and Engineering Chemistry Fundamentals*, 9(4):537–544, 1970.

[27] J. W. Leach, P. S. Chappelear, and T. W. Leland. Use of molecular shape factors in vapor-liquid equilibrium calculations with the corresponding states principle. *American Institute of Chemical Engineers Journal*, 14(4):568–576, 1968.

[28] G. J. VanWylen and R. E. Sonntag. *Fundamentals of Classical Thermodynamics*. John Wiley and Sons, Incorporated, New York, New York, 3rd edition, 1986.

[29] J. F. Ely and H. J. M. Hanley. Prediction of transport properties. 1. Viscosity of fluids and mixtures. *Industrial and Engineering Chemistry Fundamentals*, 20(4):323–332, 1981.

[30] J. F. Ely and H. J. M. Hanley. Prediction of transport properties. 2. Thermal conductivity of pure fluids and mixtures. *Industrial and Engineering Chemistry Fundamentals*, 22(1):90–97, 1981.

[31] R. B. Bird, W. E. Stewart, and E. N. Lightfoot. *Transport Phenomena*. John Wiley and Sons, Incorporated, New York, New York, 1960.

[32] S. Takahashi. Preparation of a generalized chart for the diffusion coefficients of gases at high pressures. *Journal of Chemical Engineering of Japan*, 7(6):417–420, 1974.

[33] J. C. Oefelein. Thermophysical characteristics of LOX–H_2 flames at supercritical pressure. *Prog. Combust. Inst.*, 30:2929–2937, 2005.

[34] J. C. Oefelein, R. W. Schefer, and R. W. Barlow. Toward validation of LES for turbulent combustion. *AIAA Journal*, 44(3):418–433, 2006.

[35] J. C. Oefelein. Mixing and combustion of cryogenic oxygen-hydrogen shear-coaxial jet flames at supercritical pressure. *Combust. Sci. Techn.*, 178(1-3):229–252, 2006.

[36] J. C. Oefelein, V. Sankaran, and T. G. Drozda. Large eddy simulation of swirling particle-laden flow in a model axisymmetric combustor. *Prog. Combust. Inst.*, 31:2291–2299, 2007.

[37] T. G. Drozda and J. C. Oefelein. Large eddy simulation of direct injection processes for hydrogen and LTC engine applications. *SAE World Congress, Paper 2008-01-0939*, April 14-17 2008. Detroit, Michigan.

[38] V. Sankaran, T. G. Drozda, and J. C. Oefelein. A tabulated closure for turbulent nonpremixed combustion based on the linear eddy model. *Prog. Combust. Inst.*, 32:1571–1578, 2009.

[39] B. Hu, M. P. Musculus, and J. C. Oefelein. Large eddy simulation of a transient gas jet with emphasis on entrainment during deceleration. *SAE World Congress, Paper 2010-01-1133*, April 13-15 2010. Detroit, Michigan.

[40] M. Klein, A. Sadiki, and J. Janicka. A digital filter based generation of inflow data for spatially developing direct numerical or large eddy simulations. *J. Comp. Phys.*, 186:652–665, 2003.

[41] L. M. Pickett. Engine combustion network. www.ca.sandia.gov/ECN, 2005-2011. Combustion Research Facility, Sandia National Laboratories.

[42] E.W. Lemmon, R.T. Jacobsen, S.G. Penoncello, and D.G. Friend. Thermodynamic Properties of Air and Mixtures of Nitrogen, Argon, and Oxygen from 60 to 2000 k at Pressures to 2000 mpa. *J. Phys. Chem.*, 29:331–385, 2000.